



Synergistic effect of Zr-MOF on phosphomolybdic acid promotes efficient oxidative desulfurization

Xiao-min Zhang^b, Ziheng Zhang^a, Bohai Zhang^a, Xianfeng Yang^a, Xue Chang^a, Zhen Zhou^a,
Dan-Hong Wang^{a,b,*}, Ming-Hui Zhang^{b,*}, Xian-He Bu^{a,b}

^a TKL of Metal and Molecule Based Material Chemistry, National Institute for Advanced Materials, School of Materials Science and Engineering, Nankai University, Tianjin 300350, China

^b Key Laboratory of Advanced Energy Materials Chemistry (Ministry of Education), College of Chemistry, Nankai University, Tianjin 300071, China

ARTICLE INFO

Keywords:

Phosphomolybdic acid
Zr-MOF
Oxidative desulfurization
Heteropoly blue
Mo⁵⁺

ABSTRACT

Synergistic effects between active metal species and carriers show vital importance to redox catalysts. For this study, a successful synthetic strategy is obtained from hybrid materials involving the combination of phosphomolybdic acid (PMA) and Zr-MOF. The electronic structures of the PMA/UiO-66 composites are elucidated by FTIR, Raman, XPS, UV–vis and NMR spectra. The results suggest that Mo⁵⁺ species are newly created on the composites due to the electron transfer from the conduction band of Zr-MOF to PMA. The formed Mo⁵⁺ species contribute to a high intrinsic oxidative desulfurization activity for the PMA/UiO-66 composites. Radical scavenger experiments and DFT calculations indicate that Mo⁵⁺ with rich electron density facilitates the generation of $\cdot\text{OH}$ reactive species. The approach can be employed to design other transition metal composite catalysts providing *d* electrons with unique MOF structures for enhanced catalytic activities of the redox reactions.

1. Introduction

Metal-organic frameworks (MOFs) are considered as promising and unique porous materials due to their crystalline nature, rich structural versatility and tailorability [1–4]. MOFs are constructed by nodes of metal ions/clusters and organic linkers [5–7]. Their designability can incorporate the rigidity of inorganic units with the flexibility and tunability of organic linkers [8–11]. Therefore, they have great potential in various applications, including in adsorption, separation, luminescence and catalysis processes [12–18]. Particularly, heterogeneous catalysis is suggested as the most promising application for MOFs. Some MOFs exhibit remarkable stability in liquid phase reactions permitting the recovery and reuse of the catalysts [19–21]. Compared with traditional supported catalysts, the large specific surface areas of MOFs are beneficial to the adsorption of reactants and the catalytic activities [22–24]. The periodic structures of MOFs result in a high dispersion and high density of active metal species. In addition, the metal units are structured and separated by the organic ligands, and leaching and agglomeration is less likely to occur in the catalytic reaction [25]. Despite the aforementioned merits, the low amount of active metal species in MOFs impose restrictions on the catalytic reactions. Thus, introducing various active metal species in MOFs is both urgent and interesting. The

resulting multifunctional composites may exhibit a synergistic effect, giving a full play to its function on catalytic reactions.

For the reported MOFs, the thermal stability is usually limited to 350–400 °C, while UiO-66, a type of Zr-MOF, demonstrates relatively high thermal stability with a decomposition temperature of 540 °C [26]. The inorganic unit of UiO-66 is key to its superior stability. An inner Zr₆O₄(OH)₄ octahedron core with an eight-coordinated zirconium atom are bridged by carboxylates (–CO₂) to form a Zr₆O₄(OH)₄(CO₂)₁₂ cluster (Scheme 1). The Zr₆-cluster can easily lose two μ₃–OH and two protons at just 250 °C. This results in the creation of six 7-coordinated Zr(IV) unsaturated sites [27]. Further, when Zr-MOF is treated in an inert atmosphere, a loss of lattice oxygen results in the formation of oxygen vacancies with trapped electrons [28]. These electrons trapped in the oxygen vacancy states can be easily excited to the conduction band of Zr-MOF, inducing the production of Zr(III). Zr(III) in UiO-66 composite catalysts is demonstrated to be detected at relatively low temperatures of 200–250 °C [29,30]. The reducibility makes Zr-MOF an electron donor and plays a major role in the redox reaction with a multipurpose.

Sulfur-containing organic compounds in fuels can bring about air pollution. In recent years, many regulations on the sulfur content in fuels have been applied at the ultra-low level (< 10 ppm) [31,32].

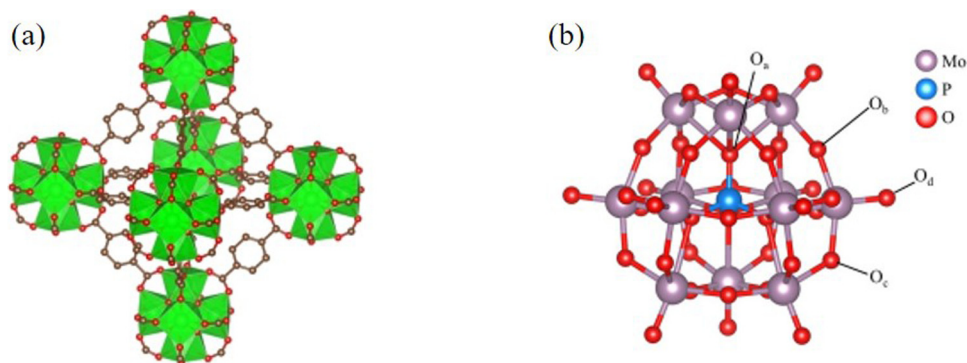
* Corresponding authors at: TKL of Metal and Molecule Based Material Chemistry, National Institute for Advanced Materials, School of Materials Science and Engineering, Nankai University, Tianjin 300350, China.

E-mail addresses: dhwang@nankai.edu.cn (D.-H. Wang), zhangmh@nankai.edu.cn (M.-H. Zhang).

<https://doi.org/10.1016/j.apcatb.2019.117804>

Received 17 November 2018; Received in revised form 27 May 2019; Accepted 30 May 2019

0926-3373/© 2019 Elsevier B.V. All rights reserved.



Scheme 1. (a) Structure of UiO-66 with a $\text{Zr}_6\text{O}_4(\text{OH})_4(\text{CO}_2)_{12}$ cluster. (b) Keggin-type structure of $\text{H}_3\text{PMo}_{12}\text{O}_{40}$ with different coordinated-oxygen.

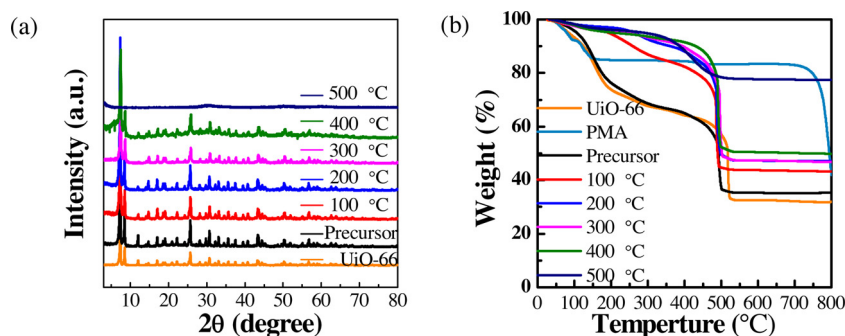


Fig. 1. (a) XRD patterns of 10% PMA/UiO-66 composites calcined at different temperatures. (b) TG curves in an N_2 atmosphere for 10% PMA/UiO-66 composites calcined at different temperatures.

Refractory sulfur compounds, for example, dibenzothiophene (DBT), particularly 4,6-dimethyldibenzothiophene (4,6-DMDBT), are difficult to be eliminated using only conventional hydrodesulfurization (HDS), which is the most widely used technique in industrial applications [33,34]. Oxidative desulfurization (ODS) has captured great attention owing to its low reaction temperature and atmospheric pressure, and high efficiency [35–37]. What is more, it is a green way to convert sulfur-containing organic compounds into oxidation products, which can be removed from oils by suitable solvent extraction or adsorption. Polyoxometalates (POMs), a type of metal oxide nanoclusters, are known to act as acid and oxidation catalysts. In particular, phosphomolybdic acid (PMA, $\text{H}_3\text{PMo}_{12}\text{O}_{40}$) is reported for the oxidation of sulfides to sulfoxide or sulfones [38–40]. Keggin-type PMA (with a molecular diameter of 1 nm) possesses characteristics that make it highly active in catalytic reactions (Fig. 1b). There are four kinds of oxygen atoms in the Keggin structure; tetrahedral oxygen (O_a) coordinated with heteroatom P, bridging oxygen (O_b) linked with different trimetallic clusters (Mo_3O_{10}), bridging oxygen (O_c) in the same trimetallic cluster, and terminal oxygen (O_d). The mobility of lattice oxygen, which is beneficial for creating oxygen vacancies, is suggested to play a constructive part in the catalytic activity [41,42]. However, there are still some challenges for POMs using in catalysis reaction. The small surface areas of POMs hinder the exposure of active sites. In addition, POMs maintain low stabilities under catalytic conditions [43,44]. To resolve these problems, many types of support, such as Al_2O_3 , carbon materials and metal-organic frameworks [45,46], have been used for the synthesis of supported POMs catalysts.

Herein, high-dispersed PMA nanoparticles are locally assembled within the structure of a typical Zr-MOF (UiO-66) (i.e., ship-in-a-bottle assembly) (Scheme 2) [47]. Strong metal-support interactions (SMSIs) is designed to be acquired between Zr-MOF (as an electron donor due to the production of Zr(III)) and PMA (as an electron acceptor due to the mobility of lattice oxygen). To our best of knowledge, investigations of ODS reactions on PMA/UiO-66 nanocomposite, are rare [48]. Another

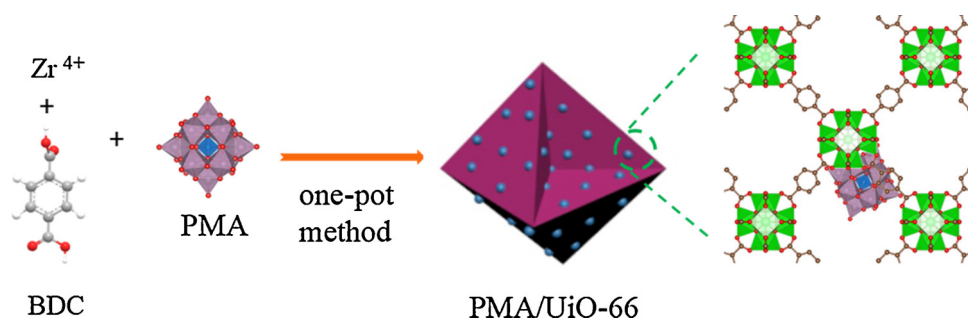
exceedingly important issue is the lack of systematic research on the relationship between catalytic efficiency and catalyst structure, and above all, the synergistic effect between PMA active species and Zr-MOF support. This study highlights that the unique structure (including electronic structure) of the PMA/UiO-66 composite can significantly increase ODS efficiency. In addition, we explore the ODS mechanism in order to discover how the synergistic effect enhances the desulfurization efficiency.

Compared to the aforementioned transition metal oxide catalysts [35,36], the PMA/UiO-66 composite demonstrates a high ODS performance with low Mo loading. The structural certainties of Zr-MOF and PMA provide convenient conditions to study the structure-activity relationship of the nanocomposite, and in turn allow us to further understanding the nature of catalytically active species from a microscopic scale.

2. Experimental section

2.1. Preparation of catalysts

Phosphomolybdic acid (PMA 23.6 mg), Phthalic acid (H_2BDC 83.5 mg), and Zirconium tetrachloride (ZrCl_4 116.5 mg) were dissolved in *N,N*-dimethylformamide (DMF 30 ml) containing Acetic acid (HAc 3.6 ml). After 30 min of sonication, the solution was diverted into a stainless steel autoclave with inner polytetrafluoroethylene, and reacted at 120 °C in a muffle furnace for 24 h. After cooling to room temperature, the solution was centrifuged, washed using DMF and Methanol, and dried at 80 °C. The precursor was activated at different temperatures in an N_2 atmosphere for 2 h using a tubular resistance furnace. Following this, 10% PMA/UiO-66 composites were obtained. The $\text{MoO}_3/\text{UiO-66}$ catalyst was prepared by substituting PMA for $(\text{NH}_4)_6\text{Mo}_7\text{O}_{24} \cdot 4\text{H}_2\text{O}$ using the same one-pot method. The catalysts are denoted as PMA-T, UiO-66-T, x% PMA/UiO-66-T, where x (2–20%) indicates the amount of PMA loading, and T represents the calcination



Scheme 2. Preparative route for PMA/Uio-66.

temperature. PMA/Uio-66-T without x% represents the PMA loading is common 10%.

2.2. Characterization of catalysts

With a scanning rate of $10^\circ/\text{min}$, X-ray diffraction (XRD) patterns were recorded in the range $3\text{--}80^\circ$ using a Rigaku MiniFlex 600 using $\text{CuK}\alpha$ radiation ($\lambda = 0.154178\text{ nm}$) at 298 K. BET results of the catalysts were obtained using an ASAP 2460 Micromeritics at 77 K after degassing for 24 h under a vacuum at 60°C . SR-500I-A Raman spectroscopy was used to measure Raman shifts of the samples at 273 K. The morphology of the samples were analyzed with a JSM-7800 F scanning electron microscope (SEM). High-resolution TEM (HRTEM) images were tested using JEM-2800 microscopy. A Bruker TENSOR-37 was used to measure Fourier transform infrared spectra at 273 K. XPS results were collected by ESCALAB 250 X-ray of Thermo Scientific. Thermogravimetric analysis (TG) was conducted using Thermo plus EVO₂ TG8121 equipment. The UV-vis measurements of the samples were carried out with a TU-1950 PERSEE. MAS NMR measurements of the samples were performed on an NMR Spectroscopy-AVANCE HD 800 MHz. Temperature-programmed reduction (H_2 -TPR) analysis was carried out with the Huasi FD-2000 thermal conductivity detector (TCD). The 50 mg catalyst was pretreated in an Ar flow (30 ml/min) at 120°C for 1 h. The reducing gas (5% H_2 in He) was then replaced with helium at the same flow rate. The temperature of the reactor increased linearly from 30 to 400°C at a rate of $5^\circ\text{C}/\text{min}$.

2.3. Catalytic reactions

A total of 0.05 g DBT was dissolved in 99.95 g decalin to form 500 ppm simulated oil. Tert-butyl hydroperoxide (TBHP) with an O/S molar ratio of 3 was then added to the simulated oil. The catalytic reaction process was performed according to the following procedure. A total of 10 g simulated diesel oil was heated to 80°C in a 50 ml round bottom flask using magnetic stirring. Subsequently, 0.05 g catalyst was added to the diesel oil, and the ODS reaction lasted for 2 h. During the reaction procedure, the solution was detected every 7 min using a gas chromatograph (GC2060) equipped with an FID detector.

2.4. Theoretical calculation methods

Density functional theory (DFT) computations were performed using the Vienna ab initio simulation package (VASP) [49]. Nuclei-electron interactions were described by the projector augmented wave (PAW), and the Perdew-Burke-Ernzerhof (PBE) form function was chosen as the electron exchange and correlation function [49–51]. The kinetic energy cut-off was set as 550 eV for the plane-wave basis set. To achieve an accurate evaluation of vander Waals interactions, the DFT-D3 method coupled with Becke-Johnson damping was adopted [52,53]. A cubic cell with the side length of 20 \AA was used for all the computation of the PMA clusters, thus preventing interactions between clusters. The Brillouin zone was sampled with only the gamma point. The

differential charge density $\Delta\rho$ is defined as:

$$\Delta\rho = \rho(\text{TBHP}/\text{PMA}) - \rho(\text{PMA}) - \rho(\text{TBHP}),$$

where $\rho(\text{TBHP}/\text{PMA})$ is the electron density of the TBHP adsorption on the PMA cluster with oxygen vacancy, and $\rho(\text{PMA})$ and $\rho(\text{TBHP})$ are the electron density of the PMA cluster with oxygen vacancy and TBHP, respectively. Bader charge analysis was also used to investigate the electron transfer between TBHP and PMA [54,55]. The figures of the structure and differential charge density were generated by VESTA [56].

3. Results and discussion

3.1. Characterization of PMA/Uio-66

XRD is used to investigate the structures of the PMA/Uio-66 composites obtained at various calcination temperatures in an N_2 atmosphere, as shown in Fig. 1a. Pure PMA maintains an $\text{H}_3\text{PMO}_{12}\text{O}_{40} \cdot 1.5\text{H}_2\text{O}$ Keggin structure (JCPDS 46-0482) until 400°C (Fig. S1), and decomposes into MoO_3 at 500°C . Pure Uio-66 can retain its MOF structure until 400°C (Fig. S2), and decomposes into ZrO_2 at 500°C . There is almost no difference between the pure Uio-66 and PMA/Uio-66 composites. In other words, the PMA crystalline phase cannot be detected from the XRD patterns, and the coating of PMA does not affect the crystal structure of Uio-66. This may provide the evidence that PMA is uniformly high-dispersed in Uio-66 for PMA/Uio-66 composites. XRD patterns of PMA/Uio-66 composites with different PMA loadings in Uio-66 (2–20%) are also only present within the diffraction peaks of Uio-66 (Fig. S3). TG (Fig. 1b) experiments were further carried out in an N_2 atmosphere in order to check the stability of the PMA/Uio-66 composites. Pure Uio-66 presents a 30% weight loss at approximately 200°C , owing to the loss of small molecular solvents (H_2O , HAc or DMF), and decomposes at approximately 520°C . All PMA/Uio-66 composites decompose at about 490°C , which is in accordance with XRD results. Above 490°C , the composite contents of remaining ash (MoO_3 and ZrO_2 verified by XRD) increases with increasing calcination temperatures. Uio-66 decomposes easily at lower temperatures in the presence of PMA, indicating that a synergistic effect between PMA and Uio-66 occurred. Similar results are observed for the $\text{MoO}_2/\text{g-C}_3\text{N}_4$ composites [35].

The IR spectra of PMA/Uio-66 composites obtained at different temperatures are shown in Fig. 2a. The spectra not only contain typical infrared bands belonging to Uio-66, but also contain Mo–O bands appertaining to PMA. Four characteristic peaks are observed for PMA in the range of $1100\text{--}400\text{ cm}^{-1}$, i.e., those at 1055 , 958 , 866 , and 786 cm^{-1} , which are attributed to the stretching vibrations of P-O_a , Mo=O_d (terminal oxygen), $\text{Mo-O}_b\text{--Mo}$ and $\text{Mo-O}_c\text{--Mo}$ (bridging oxygen), respectively. Note that increasing calcination temperatures caused a red shift for the vibration peak of Mo=O_d (958 cm^{-1}), implying that the Mo=O_d bonds became weaker. This result suggests that PMA interacts with Zr-MOF through the terminal oxygen atom O_d . According to the experimental phenomena shown in Fig. 2c, the colors

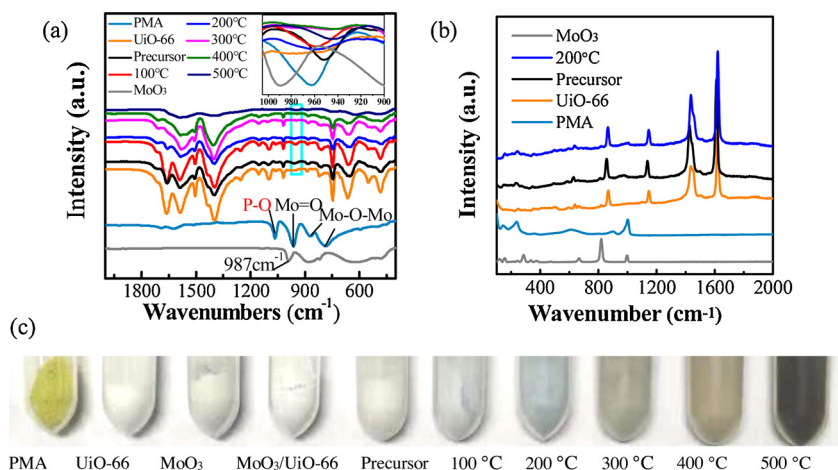


Fig. 2. (a) FTIR spectra for 10% PMA/UiO-66 composites obtained at different temperatures. (b) Raman spectra of 10% PMA/UiO-66 precursor and composite obtained at 200 °C. (c) The images of the samples (PMA, UiO-66, MoO₃, 10% MoO₃/UiO-66, 10% PMA/UiO-66 precursor and composites obtained at 100, 200, 300, 400, 500 °C).

of the composites change from yellow (PMA) to blue up to 200 °C. The corresponding heteropoly blues are likely to be attributed to the incorporation of PMA into Zr-MOF. Molybdenum heteropoly blue is a type of PMA reduction product that holds the initial Keggin structure with the exception of the color change [57,58]. In the case of the PMA/UiO-66 composites, Mo⁶⁺ ions in PMo₁₂O₄₀³⁻ may capture electrons from Zr-MOF and result in the formation of Mo⁵⁺ in the heteropoly blue. The captured electrons are delocalized in the heteropolyanion, and special redox activity for heteropoly blue is expected. Above 200 °C, the colors of the composites are darkened due to the excessive loss of lattice oxygen. Raman spectra shown in Fig. 2b also confirm that the Keggin structure PMA (1005 cm⁻¹) exists in the precursor and composite calcined at 200 °C. Temperature-dependent Raman spectra of PMA (Fig. S4) show that pure PMA can maintain a Keggin structure up until 450 °C.

According to the BET results (Table 1 and Fig. S5), the surface area and pore volume of the PMA/UiO-66 composites do not change substantially below the calcination temperature of 200 °C, demonstrating that PMA is dispersed uniformly into the UiO-66 structure. Above the calcination temperature of 200 °C, the specific surface areas and pore volumes of the composites decreased. At the temperature of 500 °C, the skeleton structure of UiO-66 collapsed according to the XRD and TG results, causing sharp drops in the surface area and pore volume.

Fig. S6 and Fig. 3 show the SEM and TEM images of the PMA/UiO-66 composites. The octahedron morphology of nanoparticles and uniform dispersion of the Mo, Zr, and P elements are detected in the PMA/UiO-66 composites. UiO-66 shows no lattice fringes under TEM conditions. The lattice fringe of the nanoclusters (with a particle size of approximately 3 nm) in the PMA/UiO-66 composites is consistent with that of PMA (JCPDS 46-0482, *d*₃₀₅ = 0.3074 nm), indicating that the PMA nanoparticles are well dispersed in UiO-66.

The electronic structures of the PMA/UiO-66 composites calcined at various temperatures are investigated using XPS analysis. Fig. 4 shows the XPS spectra and Fig. S7-8 presents the peak fitting results. Compared with pure PMA, the PMA/UiO-66 composites exhibit peaks at low

Mo_{3d} binding energies (Fig. 4a). Mo⁵⁺ (231.2 eV) is concluded to be formed in the PMA/UiO-66 composites. The PMA/UiO-66-200 presents the highest content of Mo⁵⁺ (Fig. S7), which may act as an active species in the consequent oxidative desulfurization process. Further, oxygen vacancy peaks at 532 eV are observed for the PMA/UiO-66 composites (Fig. 4b and Fig. S8). Moreover, compared with pure PMA or UiO-66, the PMA/UiO-66 composites demonstrate decreases in the binding energies of P_{2p} (Fig. 4c) together with increases in the binding energies of Zr_{3d} (Fig. 4d). This indicated that electrons transfer from Zr-MOF to the heteropolyanion PMo₁₂O₄₀³⁻. These results provide concrete evidence for strong metal-support interactions between PMA and Zr-MOF. In summary, comparing the binding energies of the PMA/UiO-66 composites with those of the UiO-66 or PMA, the O_{1s} and Zr_{3d} binding energies increase, while the Mo_{3d} and P_{2p} binding energies decrease. These results clearly prove that electron transfer occurs from Zr-MOF to PMA according to SMSIs. The detailed mechanism is described as follows: Zr-MOF easily loses lattice oxygen atoms to form oxygen vacancies with electrons trapped in (Eq. (1)) [30,59]. The energy state of the oxygen vacancy is very near to the conduction band of Zr-MOF, thus the trapped electrons are easily excited to the conduction band of Zr-MOF. Electron transfer subsequently occurs from the conduction band of Zr-MOF to the conduction band of PMA, leading to the formation of Mo⁵⁺. According to the molar ratio of Mo⁶⁺/Mo⁵⁺ summarized in Table 2, PMA/UiO-66-200 exhibits the highest Mo⁵⁺ content (Mo⁶⁺/Mo⁵⁺ = 8/4 = 2), and the (PMo₈^{VI}Mo₄^VO₄₀)⁷⁻ heteropolyanion with Keggin structure is seen to be generated in PMA/UiO-66-200 (Eq. 2). From the SMSIs between Zr-MOF and PMA, Mo⁵⁺ substitutes Mo⁶⁺ in the Keggin unit, resulting in the production of heteropoly blue, as discussed above.



UV-Vis diffuse reflectance spectra and ³¹P MAS NMR spectra are explored to further understand the electronic structures of the composites. As shown in Fig. 5, using the equation $E_g = hc/\lambda = 1240/\lambda$ (h is the Planck constant, c is the velocity of light), the band gap (E_g) of a semiconductor can be calculated from the wavelength (λ) of the absorption edge. Pure PMA and UiO-66 exhibit absorption edges at 553 nm and 320 nm, identical to the band gaps of 2.24 eV and 3.87 eV, respectively. PMA/UiO-66 composites present red-shifts of the absorption edges compared with pure UiO-66 due to the presence of PMA. Therefore, the band gap of PMA/UiO-66-200 is calculated to be 3.65 eV, slightly less than that of pure UiO-66. The adsorption bands in the region of 600–800 cm⁻¹ are attributed to the *d* electron transition of heteropoly blue containing Mo⁵⁺. Fig. 6 (a) displays the solid state ³¹P MAS NMR spectra of the PMA and PMA/UiO-66 composites using 85% phosphoric acid (H₃PO₄) as an external standard. For pure PMA, a

Table 1

Specific surface area, pore volume and pore size of the 10% PMA/UiO-66 catalysts calcined at different temperatures.

	BET (cm ² /g)	Pore Volume (cm ³ /g)	Pore size (Å)
UiO-66	1278	0.654	5.21
precursor	1279	0.66	6.07
100 °C	1165	0.66	6.29
200 °C	1241	0.69	6.62
300 °C	1031	0.57	6.00
400 °C	731	0.45	7.30
500 °C	140	0.12	374

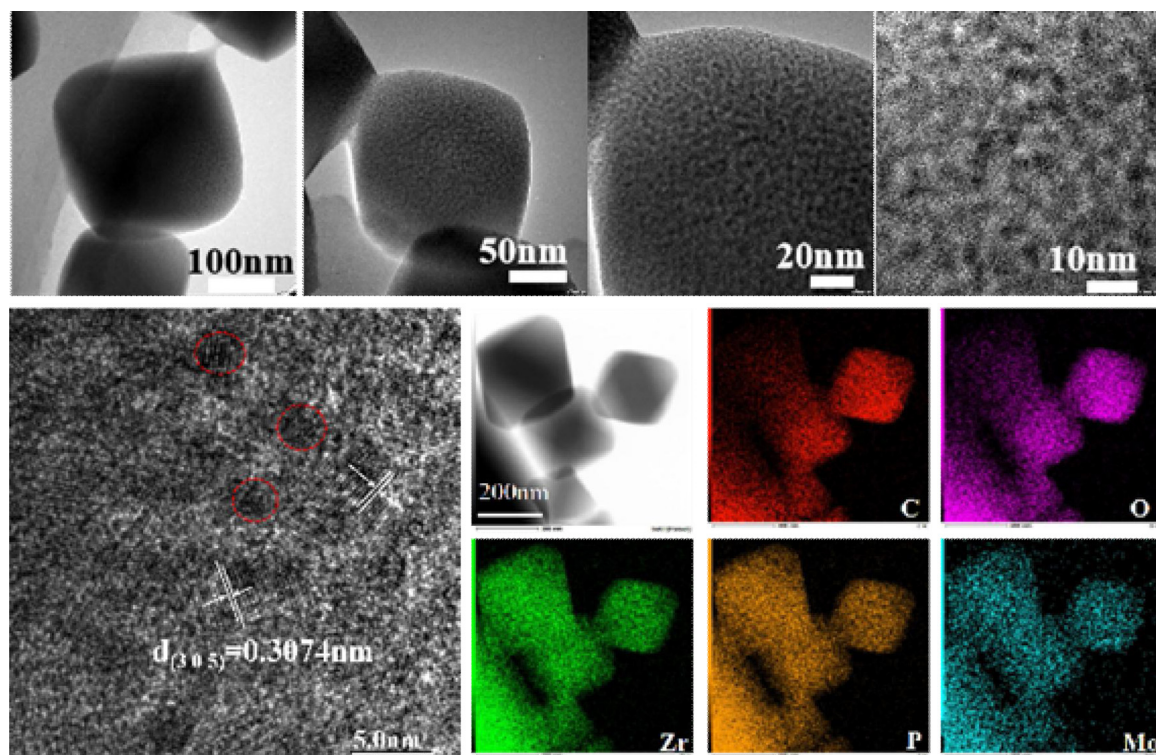


Fig. 3. TEM images and elemental mapping results of the 10% PMA/UiO-66-200 composites.

strong resonance peak at chemical shift of -6 ppm, owing to the characteristic of the PMA Keggin structure, is observed, and a shoulder peak at chemical shift of -5 ppm can be attributed to the change in the environment of the P atom with a different hydration degree [42]. The upfield shifts to -8 and -10 ppm for the precursor and PMA/UiO-66-200 composite can be attributed to the strong interaction (SMSIs) between heteropolyanion and Zr-MOF support, causing a high electron density around the P atoms. This result is consistent with the XPS results,

Table 2

The molar ratio of $\text{Mo}^{6+}/\text{Mo}^{5+}$ in the PMA/UiO-66 composites obtained by XPS.

	PMA	precursor	100 °C	200 °C	300 °C	400 °C	500 °C
$\text{Mo}^{6+}/\text{Mo}^{5+}$	11	3.5	2.7	2	4.97	5.45	11

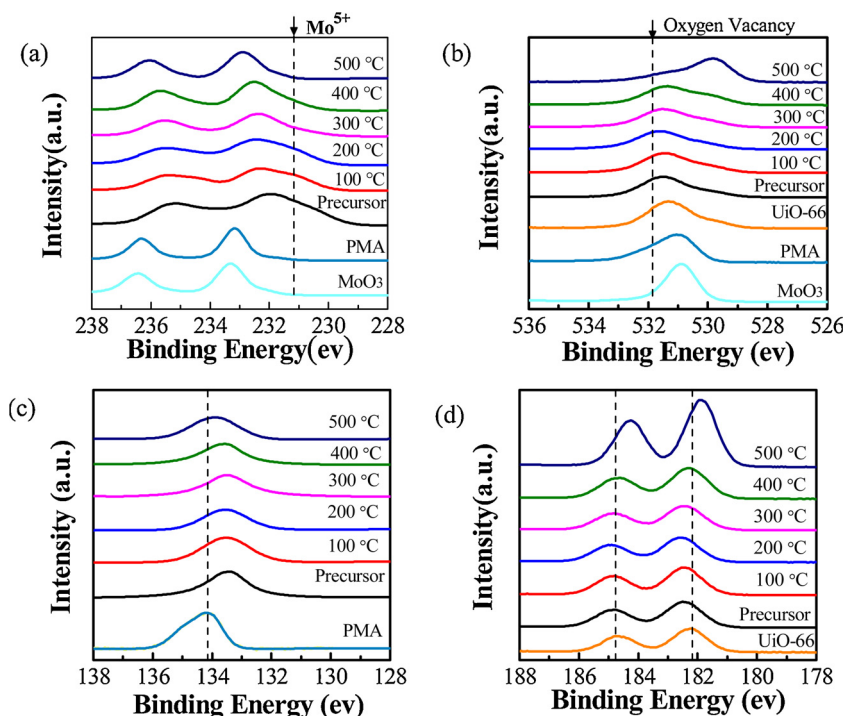


Fig. 4. XPS spectra for the PMA/UiO-66 composites obtained at different temperatures. (a) Mo_{3d} , (b) O_{1s} , (c) P_{2p} , and (d) Zr_{3d} .

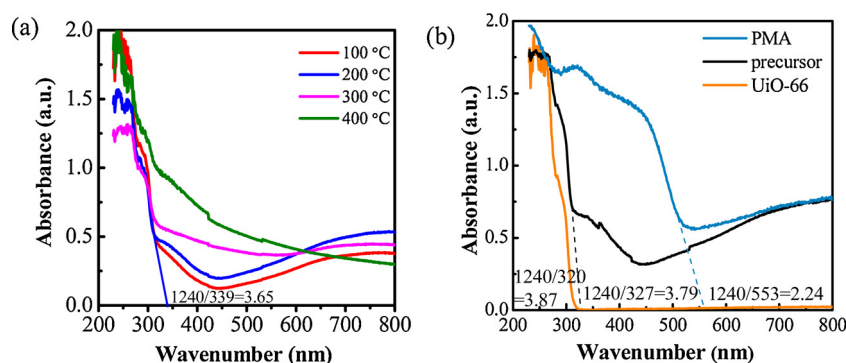


Fig. 5. UV-vis diffuse reflection spectra of (a) PMA/UiO-66 composites obtained at different calcination temperatures and (b) pure PMA, pure UiO-66 and the precursor.

whereby low P_{2p} binding energies are obtained for PMA/UiO-66 composites compared with pure PMA.

The reducibility of the catalysts was investigated using H_2 -TPR (Fig. 6b). Pure PMA showed a strong signal at 373 °C and pure UiO-66 showed a weak signal centered at 344 °C. Therefore, the precursor and PMA/UiO-66-200 present very similar reduction profiles at 365 °C and 264 °C. The peak at 365 °C (373 °C for pure PMA) were assigned to the reduction of Mo^{6+} to Mo^{5+} . The peak at 264 °C (344 °C for pure UiO-66) can be attributed to the loss of lattice oxygen in UiO-66, resulting in the formation of oxygen vacancies. According to the TPR results, Mo^{5+} and the oxygen vacancy can be easily formed in PMA/UiO-66 composites at low temperatures compared with pure PMA and pure UiO-66 [41]. This also suggests the synergistic effect between PMA and UiO-66.

3.2. Evaluation of oxidative desulfurization activities

Oxidative desulfurization performances of PMA/UiO-66 composites were tested using the oxidation of DBT and 4,6-DMDBT, with TBHP as an oxidant. We explored the effect of the reaction temperature and PMA loading on the ODS reaction, ODS activities on pure UiO-66 and PMA/UiO-66 catalysts calcined at different temperatures, and the comparison of ODS performance on MoO_3 /UiO-66-200 and PMA/UiO-66-200 (Fig. S9). Herein, in order to identify the intrinsic ODS activities for PMA/UiO-66 composites, we calculated TON values using the formula $TON = n/m$ (where n represents the mole of the reacted DBT per gram catalyst, and m represents the mole of the PMA per gram catalyst) in Fig. S9e. A key result is that the PMA/UiO-66 composite calcined at 200 °C demonstrates the highest intrinsic ODS activity in Fig. 7a and Fig. S9e. This may be related to the highest content of Mo^{5+} , as shown in Table 2. The decline in ODS performance for the composites calcined above 300 °C can be attributed to the collapse of the UiO-66 framework, resulting in the loss of surface area and pore volume, as shown in Table 1. In addition, 10% PMA/UiO-66-200 (blue color with Mo^{5+})

exhibits a much better ODS activity than 10% MoO_3 /UiO-66-200 (white color without Mo^{5+}), as shown in Fig. 2c and Fig. S9f, implying that Mo^{5+} plays a vital role in ODS activity. Therefore, the synergistic effect between UiO-66 and the active species (PMA) is further confirmed by the ODS activities.

In order to explore the specific reaction mechanism of ODS and the main reactive species over the PMA/UiO-66 catalyst, we investigated the inhibiting effect of DMSO on ODS activity with the hydroxyl radical scavenger. In Fig. 7b, the ODS efficiency drops completely in the presence of DMSO (quencher of $\cdot OH$). This result provides evidence that $\cdot OH$ is the most important reactive intermediate species in the ODS process. It is worth emphasizing that the existence of $\cdot OH$ during the ODS reaction has been proven through the EPR test on the POM catalyst [60].

In order to more vividly demonstrate the exclusiveness and superiority of the PMA/UiO-66 composite, Table 3 presents a comparison of our previous work. Note that the TON value for the PMA/UiO-66 composite is much higher than that of the MoO_2/C_3N_4 composite, indicating superior intrinsic ODS activity for the PMA/UiO-66 composite. In previous work [36], a 50% MoO_2 loading on C_3N_4 was able to reach a 100% DBT conversion in 60 min. In the metal-semiconductor heterojunction MoO_2/C_3N_4 , there was an electron transfer from the conduction band of $g-C_3N_4$ to the unfilled π^* band of the metallic MoO_2 . While, in this work, PMA/UiO-66-200 with only a 10% PMA loading was also able to reach a 100% DBT conversion in 55 min. Electrons were transferred from the conduction band of Zr-MOF to PMA, resulting in the formation of Mo^{5+} .

We also investigated the recyclability of the PMA/UiO-66 composite. The used PMA/UiO-66-200 is soaked for 48 h with methanol, centrifuged and washed several times with methanol, and dried at 80 °C for 24 h. The recycle catalyst of PMA/UiO-66-200 is reacted with a 500 ppm DBT solution under the same reaction conditions. The DBT conversion remains at 100% after three cycles, as shown in Fig. 8,

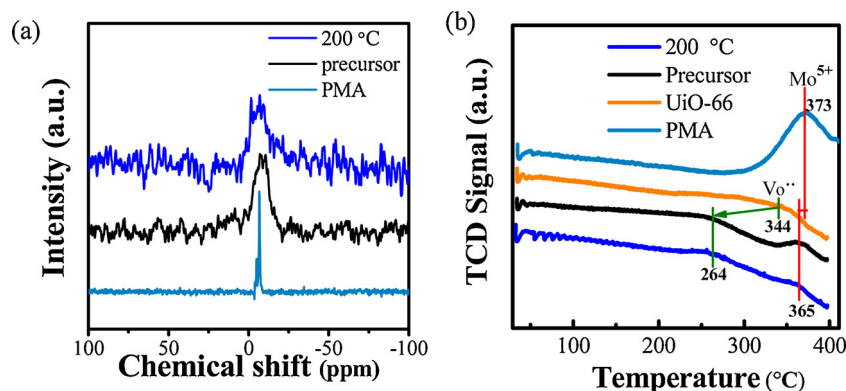


Fig. 6. (a) ^{31}P NMR spectra of the PMA and PMA/UiO-66 composites and (b) TPR results of PMA, UiO-66, the precursor and PMA/UiO-66-200.

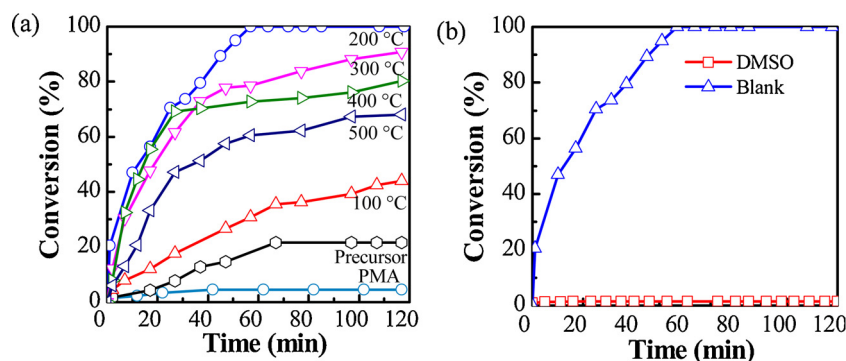


Fig. 7. (a) ODS activities over 10% PMA/UiO-66 catalysts calcined at different temperatures, (b) the inhibition effect of DMSO on the ODS reaction over the 10% PMA/UiO-66-200 catalyst.

suggesting a high recyclability. The XRD pattern for the recovered PMA/UiO-66-200 after three cycles is consistent with that for PMA/UiO-66-200, which confirms the stability of the PMA/UiO-66 composite under reaction conditions.

In order to elucidate the importance of Mo^{5+} in the PMA/UiO-66 composite on ODS activity, further DFT computation was performed for a theoretical insight of the TBHP adsorption process on PMA clusters and the effect of Mo^{5+} . The $(\text{PMo}_{12}\text{O}_{40})^{3-}$ and $(\text{PMo}_8^{\text{VI}}\text{Mo}_4^{\text{VO}}\text{O}_{40})^{7-}$ clusters were used to simulate PMA clusters without Mo(V) and with 4 Mo(V), respectively. Our results suggest that on the pristine $(\text{PMo}_{12}\text{O}_{40})^{3-}$ and $(\text{PMo}_8^{\text{VI}}\text{Mo}_4^{\text{VO}}\text{O}_{40})^{7-}$ cluster, TBHP could only bind with the hydrogen bond between the oxygen of PMA and the hydrogen of TBHP. However, when an oxygen vacancy (easy loss of terminal oxygen O_d) is introduced to the surface of the PMA cluster, TBHP adsorption is strongly enhanced by the charge transfer between the exposed Mo of PMA and the peroxy oxygen of TBHP (Fig. 9a, 8 b). The electronic interactions between TBHP and PMA were further explored by the differential charge density and Bader charge analysis. For the differential charge density (Fig. 9c, d), it is clear that the electron around Mo transfers towards the peroxy O atom with the coordination of peroxy O—O to Mo. In addition, the Bader charge analysis also suggest 0.79–0.89 eV electrons transferred from Mo to O. Furthermore, after the structural optimization, the peroxy O—O bond spontaneously breaks without any energy barrier, indicating that the oxygen vacancy greatly improves TBHP adsorption and facilitates $\cdot\text{OH}$ hydroxyl radical generation. Compared with $(\text{PMo}_{12}\text{O}_{40})^{3-}$, the binding energy of $(\text{PMo}_8^{\text{VI}}\text{Mo}_4^{\text{VO}}\text{O}_{40})^{7-}$ to TBHP is 0.17 eV high, and $(\text{PMo}_8^{\text{VI}}\text{Mo}_4^{\text{VO}}\text{O}_{40})^{7-}$ can transfer an additional 0.1 e to TBHP. Consequently, the higher electron density on Mo(V) can easily break the peroxy O—O bond, as discussed in previous work [36], leading to the easier formation of $\cdot\text{OH}$ reactive intermediate species on $(\text{PMo}_8^{\text{VI}}\text{Mo}_4^{\text{VO}}\text{O}_{40})^{7-}$. Therefore, a high ODS performance induced by the existence of Mo(V) for PMA/UiO-66-200 is obtained.

As given by the UV–vis DRS results, the band gap energies for UiO-66 and PMA are 3.87 and 2.24 eV, respectively. This is consistent with reported results (3.65 and 2.2 eV, respectively) [62,63]. Scheme 3 shows the electronic structure of the PMA/UiO-66 heterojunction and the graphical ODS mechanism on PMA/UiO-66. From the work of

[61,63], the E_{CB} of UiO-66 is approximately -0.09 eV vs. NHE, and the E_{CB} of PMA is given as 0.65 eV vs. NHE. Zr-MOF easily loses the lattice oxygen in order to form oxygen vacancies with trapped electrons. The energy level of the oxygen vacancy is close to the bottom of the Zr-MOF conduction band. Thus, the trapped electrons are easily excited to the conduction band, and transfer to a lower conduction band of PMA, forming a heterojunction. The electron transfer results in the formation of Mo(V) active species which produce an important synergistic effect on the ODS mechanism. According to the DFT calculations, the synergistic effect can be explained by the fact that TBHP can adsorb on Mo(V) to form $\cdot\text{OH}$ reactive species more easily than on Mo(VI). The formed hydroxyl radical demonstrates a strong oxidizing ability for converting 4,6-DMDBT to 4,6-DMDBTO₂ as shown in Scheme 3.

4. Conclusions

In summary, we present PMA/UiO-66 as a heterojunction composite. The nature of the synergistic effect between Zr-MOF and PMA is particularly elucidated. We draw the following conclusions:

- (1) PMA/UiO-66 composites have been successfully obtained by a facile one-pot method.
- (2) IR and Raman results show that heteropoly blue with a Keggin structure is generated due to the incorporation of PMA into Zr-MOF.
- (3) XPS results clearly indicate the formation of Mo^{5+} and an oxygen vacancy on PMA/UiO-66 composites. The $(\text{PMo}_8^{\text{VI}}\text{Mo}_4^{\text{VO}}\text{O}_{40})^{7-}$ cluster is attained on the PMA/UiO-66-200 catalyst.
- (4) UV-Vis results also suggest the formation of heteropoly blue with Mo^{5+} . NMR results indicate the strong interaction (SMSIs) between PMA and UiO-66.
- (5) TPR results reveal that Mo^{5+} and the oxygen vacancy can be more easily formed on PMA/UiO-66 composites than on pure PMA or pure UiO-66.
- (6) Electrons can transfer from the conduction band of Zr-MOF to PMA, which results in the formation of Mo^{5+} .
- (7) The PMA/UiO-66-200 catalyst displays the highest intrinsic ODS activity, which may be related to the highest content of Mo^{5+} . Mo^{5+} acted as an important active site for ODS reaction on the

Table 3
ODS activities for different catalysts in previous work and this study.

Sample	Mo Loading (%)	Calcination Temperature (°C)	DBT Conversion (%)	Reaction Time (min)	TON (mol/mol)	Reference
VO_2 (M)	Pure	500	90	120	–	[35]
$\text{MoO}_2/\text{C}_3\text{N}_4$	50	550	100	60	0.07	[36]
PMA/UiO-66	10	200	100	55	10	This study

Reaction conditions: 10 g simulated diesel oil, 0.05 g catalyst, 353 K, O/S = 3.

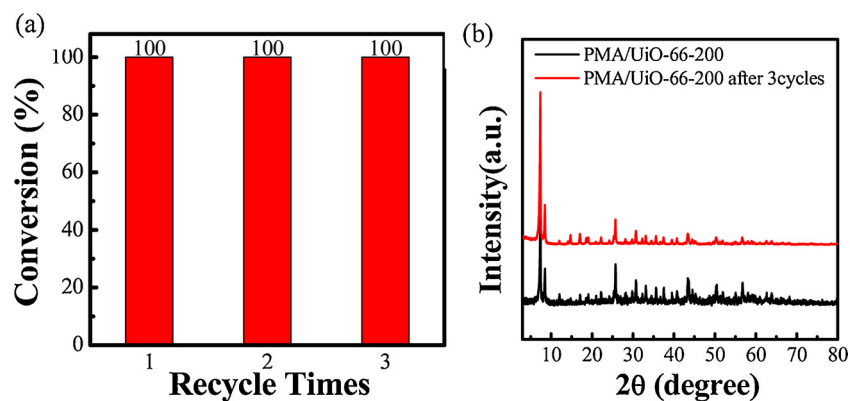


Fig. 8. ODS activities and XRD patterns of the used PMA/UiO-66-200 after three cycles.

PMA/UiO-66 composite.

- (8) Theoretical calculations provide evidence for the synergistic effect that Mo^{5+} more readily facilitates the formation of $\cdot\text{OH}$ reactive species compared with Mo^{6+} .

The achieved results open up new prospects for redox reaction using POM/MOF structures as the multifunctional catalysts.

Acknowledgments

This work was partly supported by National Natural Science Foundation of China (21421001 and 21576140), Natural Science Foundation of Tianjin (17JCYBJC20000), the Fundamental Research Funds for the Central Universities (63185015).

Appendix A. Supplementary data

Supplementary material related to this article can be found, in the

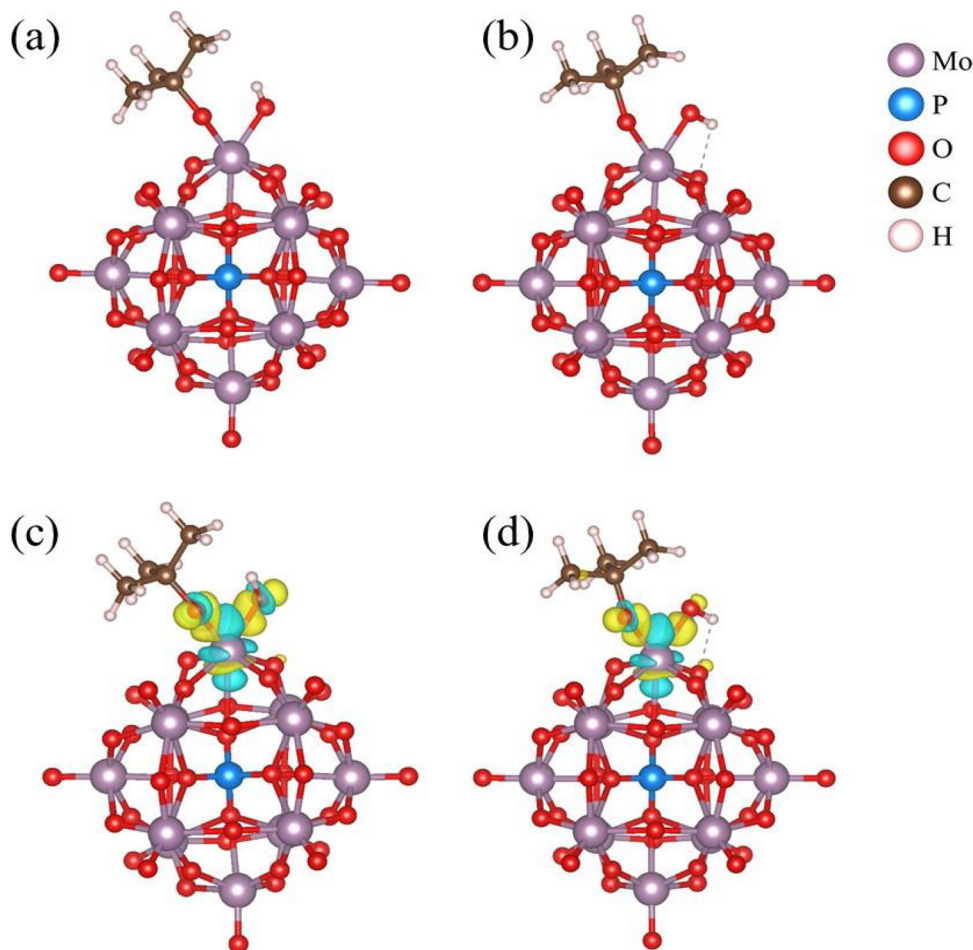
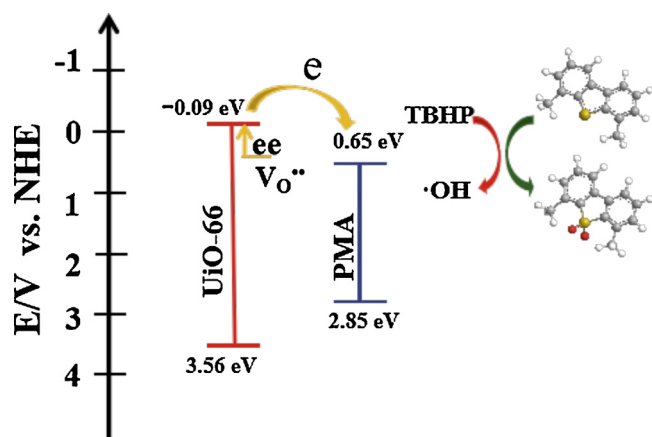


Fig. 9. (a, b) Structure and (c, d) differential charge density of TBHP adsorption on the $(\text{PMo}_{12}\text{V}_1\text{O}_{40})^{3-}$ (a, c) and $(\text{PMo}_8\text{V}_1\text{Mo}_4\text{VO}_{40})^{7-}$ (b, d) cluster with an oxygen vacancy. The blue and yellow regions indicate a decrease and increase of electrons, respectively. The isovalue is $0.015 \text{ e Bhorr}^{-3}$ (For interpretation of the references to colour in this figure legend, the reader is referred to the web version of this article.).



Scheme 3. Electronic structure of the PMA/Uio-66 heterojunction and graphical ODS mechanism.

online version, at doi:<https://doi.org/10.1016/j.apcatb.2019.117804>.

References

- G.R. Cai, H.L. Jiang, *Angew. Chem. Int. Ed.* 56 (2017) 563–567.
- O.M. Yaghi, M. O’Keeffe, N.W. Ockwig, H.K. Chae, M. Eddaoudi, J. Kim, *Nature* 423 (2003) 705–714.
- W. Zhu, G. Xiang, J. Shang, J. Guo, B. Motevalli, P. Durfee, J.O. Agola, E.N. Coker, C. Jeffrey Brinker, *Adv. Funct. Mater.* 28 (2018) 1705274(1–12).
- S. Kitagawa, R. Kitaura, S.I. Noro, *Angew. Chem. Int. Ed.* 43 (2004) 2334–2375.
- J.R. Long, O.M. Yaghi, *Chem. Soc. Rev.* 38 (2009) 1213–1214.
- G. Férey, *Chem. Soc. Rev.* 37 (2008) 191–214.
- M. O’Keeffe, M. Eddaoudi, H. Li, T. Reineke, O.M. Yaghi, *J. Solid State Chem.* 152 (2000) 3–20.
- P. Falcaro, R. Ricco, C.M. Doherty, K. Liang, A.J. Hill, M.J. Styles, *Chem. Soc. Rev.* 43 (2014) 5513–5560.
- D.J. Tranchemontagne, J.L. Mendoza-Cortes, M. O’Keeffe, O.M. Yaghi, *Chem. Soc. Rev.* 38 (2009) 1257–1283.
- S.B. Wang, W.S. Yao, J.L. Lin, Z.X. Ding, X.C. Wang, *Angew. Chem. Int. Ed.* 53 (2014) 1034–1038.
- T.H. Zhou, Y.H. Du, A. Borgna, J.D. Hong, Y.B. Wang, J.Y. Han, W. Zhang, R. Xu, *Energy Environ. Sci.* 6 (2013) 3229–3234.
- M. Eddaoudi, J. Kim, N. Rosi, D. Vodak, J. Wachter, M. O’Keeffe, O.M. Yaghi, *Science* 295 (2002) 469.
- I. Ahmed, Z. Hasan, N.A. Khan, S.H. Jung, *Appl. Catal. B* 129 (2013) 123–129.
- R. Matsuda, R. Kitaura, S. Kitagawa, Y. Kubota, R.V. Belosludov, T.C. Kobayashi, H. Sakamoto, T. Chiba, M. Takata, Y. Kawazoe, Y. Mita, *Nature* 436 (2005) 238–241.
- B. Chen, C. Liang, J. Yang, D.S. Contreras, Y.L. Clancy, E.B. Lobkovsky, O.M. Yaghi, S. Dai, *Angew. Chem. Int. Ed.* 45 (2006) 1390–1393.
- J.S. Seo, D. Whang, H. Lee, S.I. Jun, J. Oh, Y.J. Jeon, K. Kim, *Nature* 404 (2000) 982–986.
- R.Q. Zou, H. Sakurai, Q. Xu, *Angew. Chem. Int. Ed.* 45 (2006) 2542–2546.
- K.Y. Cho, J.Y. Seo, Kim H-J, S.J. Pai, X.H. Do, H.G. Yoon, S.S. Hwang, S.S. Han, Baek K-Y, *Appl. Catal. B* 245 (2019) 635–647.
- B.N. Bhadra, J.Y. Song, N.A. Khan, S.H. Jung, *ACS. Appl. Mater. Inter* 9 (2017) 31192–31202.
- D. Sun, S. Jang, S.J. Yim, L. Ye, D.P. Kim, *Adv. Funct. Mater.* 28 (2018) 1–7 1707110.
- M. Bagheri, M.Y. Masoomi, A. Morsali, *ACS Catal.* 7 (2017) 6949–6956.
- D. Farrusseng, S. Aguado, C. Pinel, *Angew. Chem. Int. Ed.* 48 (2009) 7502–7513.
- J.C. Cardoso, S. Stulp, J.F. de Brito, J.B.S. Flor, R.C.G. Frem, M.V.B. Zannoni, *Appl. Catal. B* 225 (2018) 563–573.
- Y. Liu, Z. Tang, *Adv. Mater.* 25 (2013) 5819–5825.
- K.M. Choi, K. Na, G.A. Somorjai, O.M. Yaghi, *J. Am. Chem. Soc.* 137 (2015) 7810–7816.
- J.H. Cavka, S. Jakobsen, U. Olsbye, N. Guillou, C. Lamberti, S. Bordiga, K.P. Lillerud, *J. Am. Chem. Soc.* 130 (2008) 13850–13851.
- H. Wu, Y.S. Chua, V. Krungleviciute, M. Tyagi, P. Chen, T. Yildirim, W. Zhou, *J. Am. Chem. Soc.* 135 (2013) 10525–10532.
- J.J. Zhang, Y.F. Gao, X.R. Jia, J.Y. Wang, Z. Chen, Y. Xu, *Sol. Energy Mater. Sol. Cells* 182 (2018) 113–120.
- B. An, J.Z. Zhang, K. Cheng, P.F. Ji, C. Wang, W.B. Lin, *J. Am. Chem. Soc.* 139 (2017) 3834–3840.
- B. Rungtaweeworani, J. Baek, J.R. Araujo, B.S. Archanjo, K.M. Choi, O.M. Yaghi, G.A. Somorjai, *Nano Lett.* 16 (2016) 7645–7649.
- J. Eßer, P. Wasserscheid, A. Jess, *Green Chem.* 36 (2004) 316–322.
- O. Krocher, M. Widmer, M. Elsener, D. Rothe, *Ind. Eng. Chem. Res.* 48 (2009) 9847–9857.
- C. Kwak, J.J. Lee, J.S. Bae, K. Choi, S.H. Moon, *Appl. Catal. A* 200 (2000) 233–242.
- N. Hermann, M. Brorson, H. Topsøe, *Catal. Lett.* 65 (2000) 169–174.
- K. Chen, N. Liu, M.H. Zhang, D.H. Wang, *Appl. Catal. B* 212 (2017) 32–40.
- K. Chen, X.M. Zhang, X.F. Yang, M.G. Jiao, Z. Zhen, M.H. Zhang, D.H. Wang, X.H. Bu, *Appl. Catal. B* 238 (2018) 263–273.
- J.F. Palomeque-Santiago, R. López-Medina, R. Oviedo-Roa, J. Navarrete-Bolaños, R. Mora-Vallejo, J. Ascención Montoya-de la Fuente, J.M. Martínez-Magadán, *Appl. Catal. B* 236 (2018) 326–337.
- M. Craven, D. Xiao, C. Kunzmann-Olsen, E.F. Kozhevnikova, F. Blanc, A. Steiner, I.V. Kozhevnikov, *Appl. Catal. B* 231 (2018) 82–91.
- A. Nisar, Y. Lu, J. Zhuang, X. Wang, *Angew. Chem. Int. Ed.* 50 (2011) 3187–3192.
- Y. Zhang, R. Wang, *Appl. Catal. B* 234 (2018) 247–259.
- A.M. Khenkin, L. Weiner, R. Neumann, *J. Am. Chem. Soc.* 127 (2005) 9988–9989.
- G.D. Zhou, X.M. Yang, J. Liu, K. J. Zhen, H.S. Wang, T.X. Cheng, *J. Phys. Chem. B* 110 (2006) 9831–9837.
- H. Lü, W. Ren, W. Liao, W. Chen, Y. Li, Z. Suo, *Appl. Catal. B* 138–139 (2013) 79–83.
- X.S. Wang, L. Li, J. Liang, Y.B. Huang, R. Cao, *ChemCatChem* 9 (2017) 971–979.
- J.Q. Sha, P.P. Zhu, X.Y. Yang, X.N. Li, X. Li, M.B. Yue, K.F. Zhou, *Inorg. Chem.* 56 (2017) 11998–12002.
- G. Paille, M. Gomez-Mingot, C. Roch-Marchal, B. Lassalle-Kaiser, P. Mialane, M. Fontecave, C. Mellot-Draznieks, A. Dolbecq, *J. Am. Chem. Soc.* 140 (10) (2018) 3613–3618.
- T. Wang, L. Gao, J. Hou, Servann, J.A. Herou, James T. Griffiths, W. Li, J. Dong, S. Gao, M.-M. Titirici, R. Vasant Kumar, A.K. Cheetham, X. Bao, Q. Fu, S.K. Smoukov, *Nat. Commun.* 10 (1–9) (2019) 1340.
- S.-W. Li, Z. Yang, R.-M. Gao, G. Zhang, J.-S. Zhao, *Appl. Catal. B* 221 (2018) 574–583.
- G. Kresse, J. Furthmüller, *Phys. Rev. B* 54 (1996) 11169–11186.
- G. Kresse, D. Joubert, *Phys. Rev. B* 59 (1999) 1758–1775.
- J.P. Perdew, K. Burke, M. Ernzerhof, *Phys. Rev. Lett.* 77 (1996) 3865–3868.
- S. Grimme, S. Ehrlich, L. Goerigk, *J. Comput. Chem.* 32 (2011) 1456–1465.
- S. Grimme, J. Antony, S. Ehrlich, H. Krieg, *J. Chem. Phys.* 132 (2010) 1–19 154104.
- E. Sanville, S.D. Kenny, R. Smith, G. Henkelman, *J. Comput. Chem.* 28 (2007) 899–908.
- G. Henkelman, A. Arnaldsson, H. Jónsson, *Comp. Mater. Sci.* 36 (2006) 354–360.
- K. Momma, F. Izumi, *J. Appl. Crystallogr.* 44 (2011) 1272–1276.
- M. Kozik, C.F. Hammer, L.C.W. Baker, *J. Am. Chem. Soc.* 108 (1986) 2748–1749.
- Q. Chen, C.L. Hill, *Inorg. Chem.* 35 (1996) 2403–2405.
- B. An, J.Z. Zhang, K. Cheng, P.F. Ji, C. Wang, W.B. Lin, *J. Am. Chem. Soc.* 139 (2017) 3834–3840.
- M. Romero-Sáez, A.B. Dongil, N. Benito, R. Espinoza-González, N. Escalona, F. Gracia, *Appl. Catal. B* 237 (2018) 817–825.
- J. Ding, Z.Q. Yang, C. He, X.W. Tong, Y. Li, X.J. Niu, H.G. Zhang, *J. Colloid Interf. Sci.* 497 (2017) 126–133.
- R. Karcz, P. Niemiec, K. Pamin, J. Połtowicz, J. Kryściak-Czerwenka, B.D. Napruszewska, A. Michalik-Zym, M. Witko, R. Tokarz-Sobieraj, E.M. Serwicka, *Appl. Catal. A* 542 (2017) 317–326.
- H. Zheng, C.H. Wang, X.T. Zhang, Y.Y. Li, H. Ma, Y.C. Liu, *Appl. Catal. B* 234 (2018) 79–89.